

## FLOW PREDICTION IN A PNEUMATICALLY FED IMPACT PULVERISER

Ioannis G. CHATZILAMPROU<sup>1</sup>, Mark W. YOUNDS<sup>2</sup>, Michael J. TIERNEY<sup>1</sup> and Brian ARMSTRONG<sup>3</sup>

<sup>1</sup> Bristol University, Department of Mechanical Engineering, University Walk, Bristol, BS8 1TR,  
UNITED KINGDOM

<sup>2</sup> Mountain View, Tiernaboul, Killarney, Kerry, IRELAND

<sup>3</sup> Casella CRE Energy Ltd, Stoke Orchard, Gloucestershire, GL52 4RZ, UNITED KINGDOM

Keywords: anisotropic turbulence, two-phase flow, comminution, size reduction, particle-wall impacts

### ABSTRACT

The current work has been carried out on a pneumatically fed impact pulveriser. A recent build of the proposed device, and early experiments have shown promising size reduction ratios and energy savings in comparison with conventional milling techniques.

A number of experiments have shown the points of greatest wear to be on the blades of the rotor and on the walls of the outlet duct. Experimental work was carried out on a single-phase airflow, and a two-phase air-talc mixture. Numerical simulations were performed using the proprietary CFD code FLUENT. Flow predictions of the single and two-phase systems indicated highly turbulent flows and simulations followed the trends indicated by flow visualisation. The authors propose a breakage model for particles.

### NOMENCLATURE

$C_D$	drag coefficient
$d^?$	mean particle diameter in Rosin-Rammler equation
$d_{F80}$	80% passing mesh size of feed in Bond law
$d_p$	particle diameter
$d_{P80}$	80% passing mesh size of product in Bond law
$e_n$	normal coefficient of restitution
$e_t$	tangential coefficient of restitution
$E_k$	kinetic energy
$E_{sp}$	specific energy
$F_D$	drag force
$g$	gravitational force
$k$	turbulence kinetic energy
$M$	Mach number
$m_p$	particle mass
$M_t$	turbulent Mach number
$n$	spread parameter of Rosin-Rammler equation
$p$	pressure
$R$	hydraulics radius
$S$	swirl ratio
$T$	temperature
$u$	flow velocity
$u_p$	particle velocity
$V$	control volume
$W_i$	bond work index
$Y_M$	dilatation dissipation term, for high-Mach number flows

$\alpha$	speed of sound
$\beta$	incidence angle of particle path and the wall surface, in radians
$\varepsilon$	turbulence dissipation rate
$\mu$	dynamic viscosity
$\mu'$	second coefficient of viscosity
$\Pi$	stress tensor
$\rho$	density
$\tau$	viscous stress tensor
$\omega$	angular velocity
$\bar{\Omega}$	mean rate-of-rotation tensor

### INTRODUCTION

The work presented in this paper introduces a novel method of comminution; this is an impact crusher/grinder that pulverises lumps of up to 50mm size in fractions of a second. A crude device was proposed by Francis Clute (1966), but this needed better design and scientific understanding. Following an application for a new patent (Next Century Technologies et. al., 1997), a prototype machine was manufactured in 1998, and placed in a pilot plant. Since then, new patents have been applied for (Younds et. al). To date, two projects have been completed on this system, sponsored by the European Coal and Steel Community and the Department of Trade and Industry (DTI).

The energy required to reduce 50mm lumps to powder < 100 microns is in the range of 25-125 kWh<sup>-1</sup> (Prasher, 1987). The material size reduction in these processes is achieved by impact and attrition of solid particles with a harder surface, usually made from treated and hardened steel. However, depending on the hardness of the particles appreciable wear on the impacted surface is possible. This means that machine components might have to be replaced regularly, and the product might be contaminated with metallic particles.

However, the interaction between the machine and processed material is not established. Therefore, the current work attempts for first time to achieve the mathematical/numerical modelling of this type of comminution. The main objectives of this work have been to identify the flow structure, the forces acting on solid particles, the main mechanism of breakage and possible scale-up rules for the machine. The proprietary FLUENT CFD code has been used, to predict the structures of

single-phase and two-phase flows, and to provide input for a particle breakage model.

In private communications, the following advantages have been claimed over conventional milling methods:

- High throughput rates of up to  $5.5\text{kgs}^{-1}$  in one device, which is about six times the maximum throughput of a jet mill.
- The energy requirement is approximately  $14\text{kWh}^{-1}$ , compared with  $20\text{kWh}^{-1}$  for conventional milling methods
- High size reduction ratios of up to 300:1 are achieved on a single pass, attributable to a rotor of speed up to 6000rpm
- The majority of product is less than 200 microns in diameter.
- The device is compact and has a limited number of moving parts. If the problems of rotor wear are overcome, it will need low maintenance

However, the main disadvantages to date are the high level of noise, and the potential for rotor wear. The fundamentals of operation, and the numerical model are discussed in the next sections.

The apparatus consists principally of a high-speed motor attached to a 610 mm diameter impeller (Figure 1). The motor is a 12-litre diesel engine with six cylinders in line, developing 222 kW and 105 Nm at 2000rpm. The motor drives the rotor with a belt driven twin-pulley assembly with a velocity ratio of 3:1. Attached to the impeller is a conical section and thereafter a straight duct, leading to the inlet of the apparatus. The length of the inlet duct can be changed from one to three metres, depending on the mass flow rate of the solid particles. The impellers tried so far have between eight and 12 vanes. To date, experimental results indicate that the harder is the material, the greater the number of vanes is required.

The measured velocity of the air at impeller speeds of 6000rpm is about  $250\text{ms}^{-1}$ . The inlet guide vane at the first point of impact with the particles is inclined to the left, whereas the outlet of the vane is normal to the impeller axis. Feed material is conveyed onto a scoop prior to the inlet duct section, and thereafter is accelerated into the machine. Thus, the airflow becomes anisotropic, because a swirl component of velocity occurs. The high-speed impeller transmits a weak free vortex upstream of the impeller zone. Based on preliminary work, observations from a high-speed video camera show that particles are accelerated in the inlet and conical section. However a number of localised vortices occur, as indicated by the backflow of particles in the near wall area of the conical section.

As particles are introduced to this vortex they change their path. Particles in the range of microns follow the airflow due to their low inertia. Observation of footage from a high-speed video camera indicates the following with respect to the larger particles. (1) They are likely to strike the wall of the inlet duct at some stage, (2) They are influenced by changes in the airflow, in that they tend to follow a spiral path towards the impeller vanes. After, the first impact with the impeller larger particles break,

rebound backwards to the flow, and towards the conical section wall surface, which they strike before following a path along the wall. Eventually, after a number of impacts with the walls, they hit again with the impeller, where their size is small enough to allow them to pass through and leave the domain.

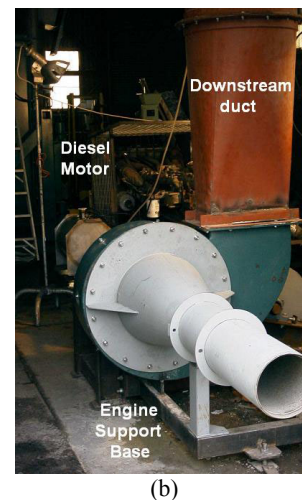
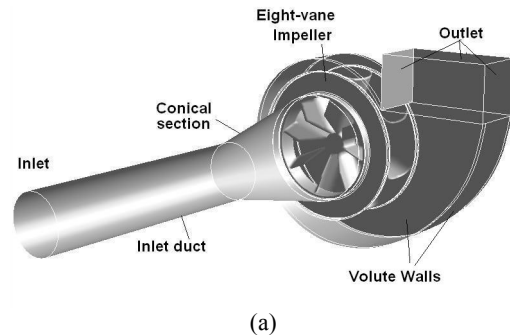


**Figure 1:** The geometrical topology of the computational domain (a) and the apparatus on site (b).

When the throughput rate is high, the big lumps, after collision with the impeller walls tend to move against the flow. It is then very likely that they hit with other particles coming from the opposite direction. This causes further size reduction, and a change in particle paths.

Downstream of the apparatus a cyclone collects the particles, where the larger particles are separated and collected at the bottom of the cyclone. The lighter particles exit the cyclone and are trapped in fabric bag filters. The filters are regularly pulsed with compressed air, and the filter cake is collected in metal bins. This way, the final size distribution includes a coarse and a fine product. (The coarse product can be fed back to the machine.) A number of experiments have shown that the assembly reduces lumps of minerals up to 50mm original diameter to a mean product particle diameter of less than 200 microns. This has applied to recycled glass, glass frit, limestone, grit-stone, talc, coal and clay.

Owing to the complexity of the physical process, computational methods are needed to solve the flow field within the domain, and investigate turbomachinery characteristics for the shape of the impeller vanes.

Additionally, two-phase flow can also be solved in terms of particle tracking. An attempt to predict the breakage mechanism of the particulate phase has been made with the same CFD code.

The numerical methods and the development of the grid and the breakage model for the two-phase flow are explained in details in the later sections.

## MODEL DESCRIPTION

The model is based around a three dimensional CAD representation of the machine. The computational domain almost matches the physical domain. In terms of flow structure, the highly turbulent flow within the physical domain necessitates high complexity in three-dimensional models. Its prediction is a state-of-art problem that needs advanced modelling functions, and a certain amount of experimental data at the boundaries. Although the standard k-ε turbulence model is very common in industrial applications, previous research (Sommerfeld, 2003, Cotton et al, 1997, Walling and Johansson, 2000) has indicated that is not capable of capturing highly swirling flows properly. The more advanced Reynolds Stress Model does this better, but at the expense of CPU-cost. As a compromise a modified version of the k-ε turbulence model, the so-called Realisable model (RKE), has been used, as discussed later. In cases where the swirl number of the flow is less than 0.5 the RKE is adequate, otherwise the Reynolds Stress Model is recommended. Additionally, for the bounded turbulent flow, at the near-wall areas the Standard Wall Functions are used (Fluent, 2002).

The consistency of the computational grid was tested in three different studies. The number of cells for each case was 114 000, 304 000 and 522 000. The numerical discrepancy between the last two cases was within two per cent, whereas in the first case it was above six per cent. Therefore, the middle case (304 000 cells) was case selected as giving the best compromise between CPU time and accuracy. In terms of CPU time, the completed two-phase flow model took approximately 28 hours on a Pentium 4 machine, with a processor speed of 1.4 GHz and 1GB memory.

For the numerical solver the Implicit Coupled solver was used. The coupled set of governing equations is discretised in time. In the steady case, the coupled solver uses the time marching until a steady-state solution is reached, (Fluent manual refers to “Time-marching for Steady-State flow, *implicit scheme*”). The system of governing equations for a single-component fluid, written to describe the mean flow properties, is cast in integral, Cartesian form for an arbitrary control volume V with differential surface area dA as follows:

$$\frac{\partial}{\partial t} \int_V W dV + \oint [F - G] dA = \int_V H dV \quad (1)$$

where the vectors W, F, and G are defined as

$$W = \begin{Bmatrix} \rho \\ \rho u \\ \rho v \\ \rho w \\ \rho E \end{Bmatrix}, F = \begin{Bmatrix} \rho v \\ \rho v u + \rho \hat{i} \\ \rho v v + \rho \hat{j} \\ \rho v w + \rho \hat{k} \\ \rho v E + \rho v \end{Bmatrix}, G = \begin{Bmatrix} 0 \\ \tau_{xi} \\ \tau_{yi} \\ \tau_{zi} \\ \tau_{xi} v_j + q \end{Bmatrix} \quad (2)$$

and the vector H contains source terms such as body forces and energy sources.

The temporal discretisation of the coupled equations is accomplished by an implicit scheme, where an Euler implicit discretisation in time of the governing equations is combined with a Newton-type linearisation of the fluxes to produce the linearised system in delta form.

For the coupling between the velocity and the pressure the SIMPLE algorithm was used, along with the second order upwind scheme for pressure and turbulent quantities, yielding higher accuracy. For the time stepping solution a Courant number of five lead to convergence.

As the velocity of the gas flow is very high, i.e. above 200ms<sup>-1</sup>, Mach number is bigger than 0.3, thereafter the compressibility effects are encountered and in which large pressure variations are experienced. Therefore, in all three cases, the flow was compressible, using the ideal-gas law, and the flow field solved in the steady state. The flow is viscous and the identity of the fluid passing through a control volume changes with the time. The transport equations of mass, momentum, and energy, without turbulence quantities, were solved with reference to a Cartesian co-ordinate system (x, y, z) in a three-dimensional domain. The continuity equation for each co-ordinate followed the form of Equation 1. A special, form is found if Newton’s Second Law is applied to the control volume. This yields the following momentum equation, in differential form.

$$\frac{\partial}{\partial t}(\rho V) + \nabla \cdot \rho V V = \rho f + \nabla \cdot \Pi_{ij} \quad (3)$$

The first term represents the rate of increase of momentum per unit volume in the control volume, whereas the second term is the rate of momentum lost by convection through the control surface. On the right-hand side, the first term is body force per unit volume. Body forces, i.e. gravitational force, act at a distance and apply to the entire mass of the fluid. The second term is the surface forces per unit volume, stresses, which are consisted of normal and shearing stresses.

Based on the Newtonian fluid assumption a general deformation law derived by Schlichting (1979), which relates the stress tensor to the pressure and velocity components. The stress tensor is written in the following form:

$$\Pi_{ij} = -p \delta_{ij} + \mu \left[ \left( \frac{\partial u_i}{\partial x_j} + \frac{\partial u_j}{\partial x_i} \right) + \frac{2}{3} \delta_{i\epsilon} \frac{\partial u_k}{\partial x_k} \right] \quad (4)$$

where (i, j, k = 1,2,3)

The  $\delta_{ij}$  is the Kronecker delta function ( $\delta_{ij}=1$  if  $i=j$  and  $\delta_{ij}=0$  if  $i \neq j$ ), and the dynamic viscosity is related to the second coefficient of viscosity, as

$$\mu = 1.5 \mu' \quad (5)$$

as the bulk viscosity is negligible. The second term is equivalent to the viscous stress tensor  $\tau_{ij}$ .

$$\tau_{ij} = \mu \left[ \left( \frac{\partial u_i}{\partial x_j} + \frac{\partial u_j}{\partial x_i} \right) + \frac{2}{3} \delta_{ij} \frac{\partial u_k}{\partial x_k} \right] \quad (6)$$

(i, j, k = 1,2,3)

By combining equations 3,4 and 5 we get the full Navier-Stokes equations.

$$\rho \frac{Du}{Dt} = \rho f_x - \frac{\partial p}{\partial x} + \frac{\partial}{\partial x} \left[ \frac{2}{3} \mu \left( 2 \frac{\partial u}{\partial x} - \frac{\partial v}{\partial y} - \frac{\partial w}{\partial z} \right) \right] + \frac{\partial}{\partial y} \left[ \mu \left( \frac{\partial u}{\partial y} + \frac{\partial v}{\partial x} \right) \right] + \frac{\partial}{\partial z} \left[ \mu \left( \frac{\partial w}{\partial x} + \frac{\partial u}{\partial z} \right) \right] \quad (7)$$

$$\rho \frac{Dv}{Dt} = \rho f_y - \frac{\partial p}{\partial y} + \frac{\partial}{\partial x} \left[ \mu \left( \frac{\partial v}{\partial x} + \frac{\partial u}{\partial y} \right) \right] + \frac{\partial}{\partial y} \left[ \frac{2}{3} \mu \left( 2 \frac{\partial v}{\partial y} - \frac{\partial u}{\partial x} - \frac{\partial w}{\partial z} \right) \right] + \frac{\partial}{\partial z} \left[ \mu \left( \frac{\partial v}{\partial z} + \frac{\partial w}{\partial y} \right) \right] \quad (8)$$

$$\rho \frac{Dw}{Dt} = \rho f_z - \frac{\partial p}{\partial z} + \frac{\partial}{\partial x} \left[ \mu \left( 2 \frac{\partial w}{\partial x} + \frac{\partial u}{\partial z} \right) \right] + \frac{\partial}{\partial y} \left[ \mu \left( \frac{\partial v}{\partial z} + \frac{\partial w}{\partial y} \right) \right] + \frac{\partial}{\partial z} \left[ \frac{2}{3} \mu \left( 2 \frac{\partial w}{\partial z} - \frac{\partial u}{\partial x} - \frac{\partial v}{\partial y} \right) \right] \quad (9)$$

The energy equation is given in its general form as follows:

$$\frac{\partial E_t}{\partial t} + \nabla \cdot E_t V = \frac{\partial Q}{\partial t} - \nabla \cdot q + \rho f \cdot V + \nabla \cdot (\Pi_{ij} \cdot V) \quad (10)$$

In equation (10) above, the first term on left-hand side is the rate of increase of total energy per unit volume in the control volume while the second term is the rate of total energy lost by convection (per unit volume) through the control surface. On the right-hand, the first term represents the rate of heat produced per unit volume by external sources while the second term is the rate of heat lost by conduction (per unit volume) through the control surface. The third term presents the work done on the control volume by the body forces while the fourth term represents the work done on the control volume by the surface forces. For a Cartesian coordinate system it takes the following form:

$$\begin{aligned} & \frac{\partial E_t}{\partial t} - \frac{\partial Q}{\partial t} - \rho(f_x u + f_y v + f_z w) + \\ & \frac{\partial}{\partial x} (E_t u + p u - u \tau_{xx} - v \tau_{xy} - w \tau_{xz} + q_x) + \\ & \frac{\partial}{\partial y} (E_t v + p v - u \tau_{xy} - v \tau_{yy} - w \tau_{yz} + q_y) + \\ & \frac{\partial}{\partial z} (E_t w + p w - u \tau_{xz} - v \tau_{yz} - w \tau_{zz} + q_z) = 0 \quad (11) \end{aligned}$$

## Turbulence Modelling

The physics of the flow structure is turbulent as many vortices are created within the conical section due to the impeller rotation. The swirl number of the flow which is defined as the ratio of the axial flux of angular momentum to the axial flux of the axial momentum is given by

$$S = \frac{\int r \omega v dA}{R \int u v dA} \quad (12)$$

The *Realisable model* is a modified k- $\varepsilon$  turbulence model. (Shih et al., 1995). It satisfies certain mathematical constraints on the normal Reynolds stresses, consistent with the physics of turbulent flows. It has a remarkable performance over the standard k- $\varepsilon$  model, especially for separated and complex flows with secondary features. The general transport equations for  $k$  and  $\varepsilon$  are given by:

$$\rho \frac{Dk}{Dt} = \frac{\partial}{\partial x_j} \left[ \left( \mu + \frac{\mu_t}{\sigma_k} \right) \frac{\partial k}{\partial x_j} \right] + G_k + G_b - \rho \varepsilon - Y_M \quad (13)$$

$$\begin{aligned} \rho \frac{D\varepsilon}{Dt} = & \frac{\partial}{\partial x_j} \left[ \left( \mu + \frac{\mu_\varepsilon}{\sigma_\varepsilon} \right) \frac{\partial \varepsilon}{\partial x_j} \right] + \rho C_1 S \varepsilon - \\ & \rho C_2 \frac{\varepsilon^2}{k + \sqrt{\nu \varepsilon}} + C_{1\varepsilon} \frac{\varepsilon}{k} C_{3\varepsilon} G_b \end{aligned} \quad (14)$$

$$\text{where} \quad C_1 = \max [0.43, (\eta/(\eta+5))] \quad (15)$$

$$\text{and} \quad \eta = S k / \varepsilon \quad (16)$$

In these equations  $G_k$  represents the generation of turbulent kinetic energy due to the mean velocity gradients, whereas,  $G_b$ , is the generation of turbulent kinetic energy due to buoyancy. The term,  $Y_M$  is the contribution of the dilatation in compressible turbulence to the overall dissipation rate,  $C_{1\varepsilon}$ ,  $C_{2\varepsilon}$ , are constants and  $\sigma_k$ ,  $\sigma_\varepsilon$  are the turbulent Prandtl numbers for  $k$  and  $\varepsilon$ , respectively. Unlike the standard k- $\varepsilon$  model, the variable  $C_\mu$  is not constant and is given by:

$$C_\mu = \frac{1}{A_0 + A_s \frac{U^* k}{\varepsilon}} \quad (17)$$

$$\text{where} \quad U^* = \sqrt{S_{ij} S_{ij} + \tilde{\Omega}_{ij} \tilde{\Omega}_{ij}} \quad (18)$$

and

$$\tilde{\Omega}_{ij} = \Omega_{ij} - 2 \varepsilon_{ijk} \omega_k, \quad \Omega_{ij} = \overline{\Omega_{ij}} - \varepsilon_{ijk} \omega_k \quad (19)$$

$\overline{\Omega_{ij}}$  is the mean rate-of-rotation tensor viewed in a rotating frame of reference with the angular velocity  $\omega_k$ . The constants  $A_0$  and  $A_s$  are given by:

$$A_D = 4.04 \quad A_S = 6^{0.5} \cos \varphi \quad (20)$$

$$\text{and} \quad S_{ij} = \frac{1}{2} \left( \frac{\partial u_j}{\partial x_i} + \frac{\partial u_i}{\partial x_j} \right) \quad (21)$$

where

$$\phi = \frac{1}{3} \arccos(\sqrt{6}W), \quad W = \frac{S_{ij}S_{jk}S_{ki}}{\tilde{S}}, \quad \tilde{S} = \sqrt{S_{ij}S_{ij}}, \quad (22)$$

Therefore it can be seen that the variable  $C_\mu$  is a function of the mean strain and rotation rates, the angular velocity of the system rotation, and the turbulence fields ( $k$  and  $\varepsilon$ ). In equation 13 the term  $Y_M$  applies when compressibility affects turbulence at high-Mach number flows, and is given by:

$$Y_M = \rho \varepsilon 2(M_t)^2 \quad (23)$$

where  $M_t$  is the turbulent Mach number:

$$M_t = (k/\alpha^2)^{1/2} \quad (24)$$

Moreover, the variables  $G_k$  and  $G_b$ , explained above take the following form when the ideal gas law is applicable:

$$G_k = -\rho \overline{u_i u_j} \frac{\partial u_j}{\partial x_i} \quad (25)$$

$$G_b = -g_i \frac{\mu_i}{\rho Pr_i} \frac{\partial \rho}{\partial x_i} \quad (26)$$

The constants in the Realisable  $k$ - $\varepsilon$  model are as follows:

$$C_{1\varepsilon}=1.44, \quad C_2=1.9, \quad \sigma_k=1.0, \quad \sigma_\varepsilon=1.2, \quad Pr_t=0.85$$

and

$$C_{3\varepsilon} = \tanh\left|\frac{v}{u}\right|,$$

where  $v$  is the component of the flow velocity parallel to the gravitational vector and  $u$  the one which is perpendicular to it.

### Mesh Generation

The three-dimensional computational domain was constructed from a collection of tetrahedral, triangular prisms, and hexahedral cells. The numerical model consisted of 304 000 cells (Fig. 1). Five block-volumes were generated separately in three sub-domains, wherein different mesh schemes applied. The sub-domains were: (1) the inlet duct plus the conical section (2) the impeller (3) the volute plus the outlet.

The sub domains were later merged to produce the final computational domain.

The first two sub domains were meshed with unstructured hexahedral elements, applying the Cooper scheme, which mirrors surface meshes in a three-dimensional volume block. The mesh at the near-wall area was dense to capture eddies and secondary flows in the conical section. In the impeller sub domain, where the geometry was complex, (Fig. 3) a number of volumes from the original CAD output were merged with each other to create "virtual volumes" (Fluent, 2002), which were easier to mesh. Tetrahedral elements, which are equipped with a set of size functions, provided a good control of the grid in areas of high density.

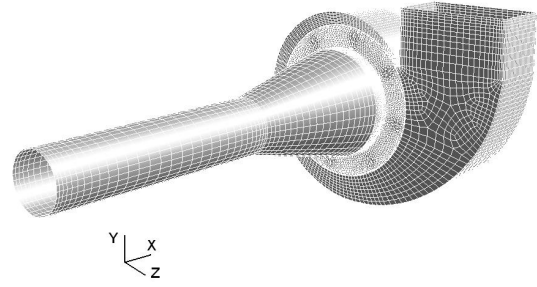
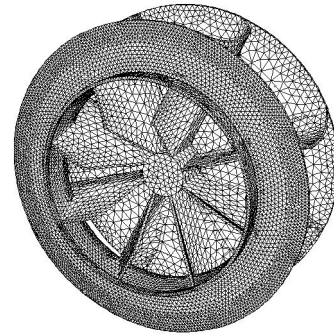


**Figure 2:** The boundary grid of the computational domain.

At the interfaces between sub domains, prisms were generated from the existing quadrilateral surface mesh. In sub domain (3) a block-structured mesh applied, with hexahedral elements, using the Cooper scheme. The mesh was quite dense near the leading and trailing edge of the vanes of the impeller; experimental work had shown wear in that area. The mesh was dense at the outlet, where backflow was likely to occur at the near-wall area. The worst skewness was found in six tetrahedral elements, and was 0.88.



(a)



(b)

**Figure 3:** The concurrency of the topology and the boundary mesh of the impeller (a).

### Boundary Conditions

Pressure-inlet and pressure-outlet boundary conditions were applied to the inlet and outlet. Static and total pressure, total temperature and velocity direction, as well the turbulence intensity and the hydraulic diameter, were the necessary inputs. The zone of the impeller was selected to rotate at 5555 rpm anti-clockwise, around the X-axis. For the velocity components the Cartesian coordinate system used, resembling that of the left-hand rule. The origin was placed on the principal axis of the

inlet duct. Fluent provides for backflow at the outlet boundary, so all the values are shown in the table below.

CFD Run	Inlet	Outlet
Static pressure (Pa)	60 000	102 000
Total pressure (Pa)	110 000	-
Total temperature (K)	317.5	307.44
Turbulence intensity, (%)	2	5
Hydraulic diameter, (m)	0.22	0.22

**Table 1:** Modelling conditions.

For the fluid zone of the impeller the Rotating Reference Frame (RRF) technique was chosen. Here the walls of the machine were considered as rotating, at speed  $r \cdot \omega$ , where  $r$  is the radial distance of a point from the central axis, and the impeller was considered to be static. (The converse would be true for the absolute frame of reference).

## TWO-PHASE FLOW MODELLING

In a two-phase flow problem there are two approaches available in the literature, the Euler-Lagrangian, and the Euler-Euler. In the former, the gas phase is treated as a continuum by solving the time-averaged Navier-Stokes equations. The secondary phase is solved by tracking a large number of particles, bubbles or droplets through the calculated flow field. Depending on the mass-loading ratio, the two phases can be coupled so as to exchange momentum, mass and energy. The criterion for a coupled two-phase flow solution is a value of the mass loading larger than 0.2. Even though the mass loading can be higher than unity, however, this approach is limited to a low volume fraction of the secondary phase, 10% at maximum. The approach can be useful for processes such as in pneumatic conveying.

In the Euler-Euler approach the different phases are treated mathematically as interpenetrating continua. Since the volume of a phase cannot be occupied by the other phases, the concept of phase volume fraction is introduced. The volume fractions are assumed to be continuous functions of space and time; their sum is equal to one. A set of conservation equations for each phase is, with similar structure. These equations are closed by providing constitutive relations that are obtained from empirical information or in the case of granular flows, by the application of kinetic theory.

In the current work, the particle-wall collisions in a dilute dispersed-phase flow were simulated using the former approach. The particle trajectories were calculated by solving the momentum equations in the three dimensional Cartesian system:

$$\frac{du_p}{dt} = F_d(u - u_p) + \frac{g_i(\rho_p - \rho)}{\rho_p} \quad (27)$$

where  $i = x, y, z$ .

The *drag force* is written as

$$F_D = \frac{18\mu C_D}{\rho_p d_p^2} \frac{\rho d_p}{24} \frac{|u_p - u|}{\mu} \quad (28)$$

where  $\rho d_p |u_p - u| \mu^{-1}$  is the particle Reynolds number,  $Re_p$ .

The drag coefficient  $C_D$  is calculated based on high-Mach number law, applicable to a particle Mach number greater than 0.4 and a particle Reynolds number greater than 20. It includes the correlations on the Standard Drag Curve for a spherical particle (Clift et. al., 1978).

Also, the rotational inertia of particles, body forces due to the rotation frame of the impeller, and due to the pressure gradient of the airflow are not considered. Also, Brownian forces are ignored; this is reasonable for particle sizes greater than one micron.

The simulated throughput rate of the dispersed phase was  $1.0 \text{ kgs}^{-1}$ . The material modelled was Talc, with a density of  $27000 \text{ kgm}^{-3}$ . Data on the feed size distribution was obtained after sieve analysis on site. The mass-loading ratio was less than 0.2, therefore the dispersed flow was not strongly coupled with the airflow. Thus, the solid phase only influenced the airflow weakly. Heat transfer is small, and there is no evaporation or chemical reaction, so no mass transfer. Momentum transfer, or inter-phase drag, would have influence particle trajectories.

The particle size varies from 38-30 000 microns, and the size distribution is given by a Rosin-Rammler distribution, as follows:

$$F(d_p) = 1 - \exp[-(d_p / d')^n] \quad (29)$$

Note that this gives a proportion of material below size  $d_p$  (the undersize), whereas Fluent manual gives a form relating to the proportion of material above size  $d_p$  (the oversize).

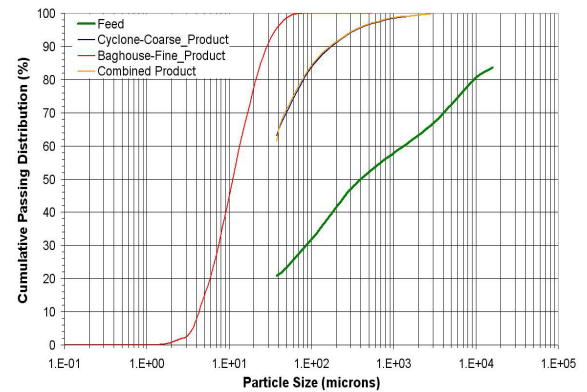


**Figure 4:** Particle size distribution at the inlet of the computational domain, as used in the simulation. The feed size distributions presented by a Rosin-Rammler equation.

The mean diameter  $d'$  is calculated for that diameter value when  $F(d_p) = 1 - \exp^{-1} = 0.632$ , and as it is shown in figure 4,  $d' \sim 1700 \mu\text{m}$ . Modifying equation (29) to calculate the spread parameter  $n$ , for each size interval of the feed distribution, yielded an average value of 0.379.

Figure 4, also shows the size distributions of product in outlets, the cyclone and the bag house. The particles are assumed to be introduced to the computational domain with a uniform velocity of  $1 \text{ ms}^{-1}$ , in the axial direction.

## PARTICLE-WALL IMPACT MODEL

The proposed particle-wall impact model, is a simple breakage model, and tends to predict the main breakage mechanism of the particles, as well as areas, where wear is likely to occur. It should be noted that the rotor blades do wear; in some experiments the mineral has made large holes in them. The mass loadings here have varied from 0.833 to 5.555 kgs<sup>-1</sup>.

For reasons of simplicity, the particle shape is treated as spherical. Based on the product size distribution, the measured flow velocities within the domain, and snapshots from high-speed video, the main mechanism of breakage is thought to be impact rather than attrition, compression or shear. Whilst tiny levels of attrition might occur between the outlet and the sampling point downstream of the cyclone, the measured particle size distribution is thought to represent the outlet material adequately.

For the numerical particle tracking 12 injection groups were initialised at the inlet boundary face from different location points. Each group was visualised with 30 particle streams, that is 30 equal size intervals of the feed size distribution. For the modelling of the turbulent dispersion of the dilute dispersed phase, each particle trajectory was calculated 30 times to include the fluctuations of the turbulent flow field on a particle path. That results in 900 particle tracks for each injection group. Every injection has a total mass flow of 0.0833 kgs<sup>-1</sup> thus, the total mass flow rate of the dilute dispersed phase is 1.0 kgs<sup>-1</sup>. A large number of trajectories is required for meaningful results (Chen, and Pereira, 1997), 10800 trajectories in the current case. For the impacts at wall surfaces the profiles of normal and tangential coefficients of restitution have been calculated according to the work of Tabakoff et. al. (1987) for targeting a mild-steel wall,

$$e_n = 0.993 - 1.76\beta + 1.56\beta^2 - 0.49\beta^3 \quad (30)$$

$$e_t = 0.998 - 1.66\beta + 2.11\beta^2 - 0.67\beta^3 \quad (31)$$

The incidence angle  $\beta$  is in radians in the profiles above.

For fine grinding the high velocities between the particles and the grinding medium are necessary. Herein, it is assumed that when a particle collides with a wall at a high velocity, the kinetic energy is completely converted into fracture energy:

$$E_k \sim 0.5 m_p u_p^2 \quad (32)$$

Using the user defined functions of the CFD software the main assumption of the breakage modelling is that after a particle collides with a wall-surface its diameter does not change. The number of impacts on each wall zone may be used to early predict the main breakage mechanism and also to show wall-surfaces where erosion is likely to occur due to the large number of impacts.

## RESULTS AND DISCUSSION

Results for single phase and two-phase simulations are presented here.

Air velocities and temperatures were measured at several locations within the machine; data extracted near the inlet and the outlet are reported here. At the inlet the sample points were located 44mm from the wall, and were located

azimuthally and equispaced. Because of likely edge effects at the inlet (possibly expansion or recirculation) the points of measurement were located 70mm downstream from the actual inlet face. The recorded pressure were total values - table 1 shows them alongside static values estimated on the assumption of isentropic flow.

The pressure probes were connected to piezoelectric sensors. Temperatures were measured with thermocouples attached to 6mm diameter tubes to ensure strength, and introduced through the machine wall.

The predicted flow field is presented in Figures five-nine where contours of total pressure, total temperature, and Mach number are shown on the wall surfaces of the domain. For both pressure and temperature, the highest values were indicated on the suction-side, near the shroud of the impeller. The pressure increases along the impeller radius until the impeller shroud, whereas, the temperature along the reverse direction of the X-axis, towards the vane-impeller wall. Regarding the Mach number, the inlet duct is similar to a converging-diverging nozzle.

In figure 6, is shown the pressure increase over the impeller due to the added work. It can be seen that the highest values of pressure exist at the suction-side-shroud of the impeller, in particular, where the tip-clearance of the impeller casing starts to increase.

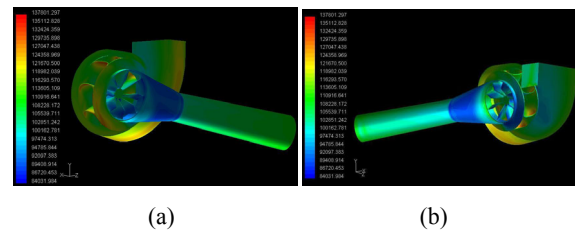


**Figure 5:** The total pressure contours on the domain walls from left (a) and right (b) view show the high-pressure areas to be on the suction-side-shroud of the impeller.

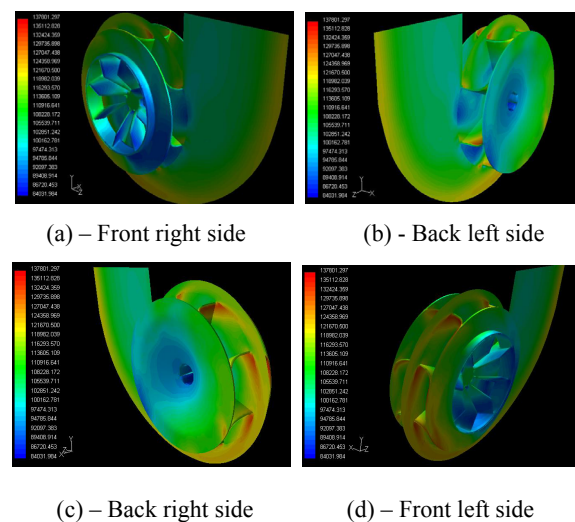


**Figure 6:** The total pressure on the impeller walls and on a visual surface at the mid-span of the impeller. Four different isometric views show the difference in total pressure areas.

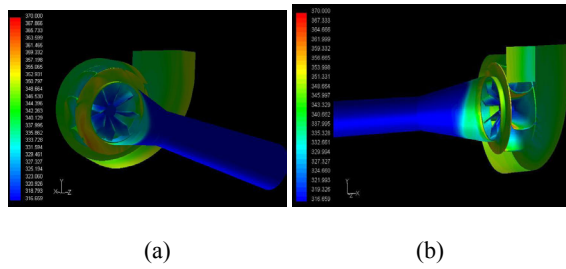


**Figure 7:** The total temperature contours on the domain walls from left (a) and right (b) view show the high-pressure areas to be on the suction-side-shroud of the impeller.

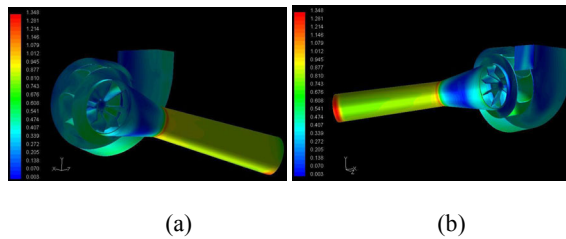


**Figure 8:** The Mach number from left (a) and right (b) view shows the choked flow at the inlet face and just before the inlet duct end.

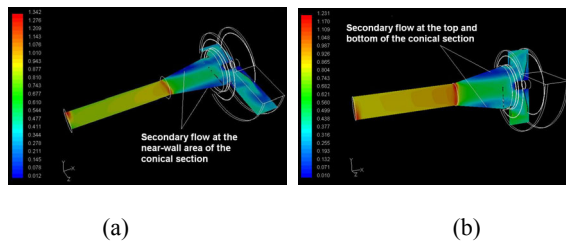


**Figure 9:** Mach contours of two section areas throughout the domain along the Y and Z-axis indicate separation and vortices at the near-wall area in the conical section.

The velocity contours on Figure 8 indicate the separation flows that occur at the near-wall area of the conical section, in two sections of the domain along the Y and Z-axis, respectively.

Measured and computed pressures are in fair agreement (Figure 10). The numerical error shown is within 2.29 and 1.39 %, respectively. The small area of the inlet face shows where some flows were choked at the inlet, indicating air speeds at of roughly  $300 \text{ m.s}^{-1}$ . The axial velocity of component of velocity would have been less than this. Because  $M > 1$  before the conical section, there is an anisotropic and inhomogeneous turbulence, which needs special conditions, as provided by Chen (Chen, 2000). Despite this, the choking of the flow does not appear, from CFD visualisations, to seriously affect the flow structure downstream. A better profile including more points at both the actual inlet and the point 70mm downstream will be measured in future to assist the numerical modelling.

In general, the modified two-equation  $k-\epsilon$  turbulence model, RKE, has predicted the swirl flow well, however, the advanced Reynolds Stress Model may be used for further comparisons.

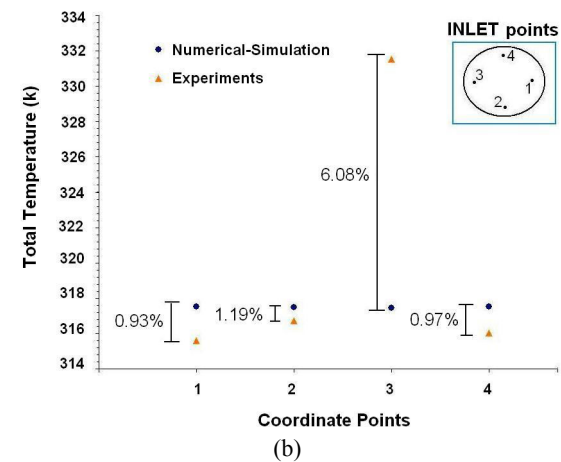
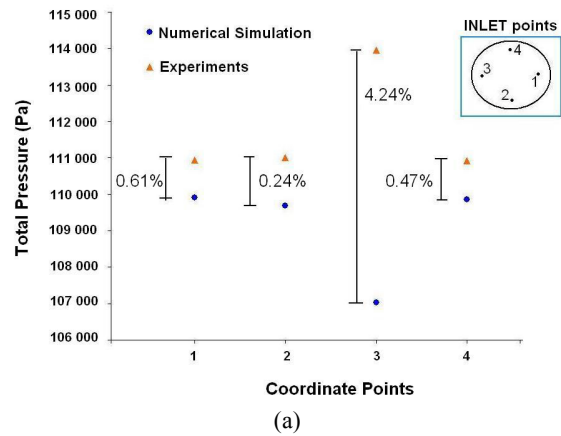


**Figure 10:** Experimental and numerical comparison of the inlet coordinates for pressure (a) and temperature (b); numerical error shown in the graphs.

To give some checks on the predictions from the two-phase flow model, a KODAK EM High Speed Video Camera was used, set at 500 frames per second for capturing single particles of five up to 50mm size. The videos were recorded on a VHS tape and then transferred to a computer for further analysis. A number of small digital images were generated for each particle indicated that the direction of the particle in the inlet duct is independent of its size. The particle trajectory is an almost straight line downstream the inlet until the end of the duct. In the conical section the small particles followed an apparently random path owing to their small inertia and the number of vortices. As the particle size increased the particle track in the conical section seemed to be parabolic towards the impeller, where the particle collided. The big lumps tended to rebound and move opposite to the flow direction and follow a spiral orbit along the conical section wall. This phenomenon was observed in the numerical modelling of the two-phase flow, and the secondary flows occur to the near-wall area.

Both camera observations and CFD predictions showed that in the inlet duct, particles tended to move almost in a straight line, until their collision with the impeller. Therefore, by capturing the predicted particle velocity, size and the time at the plane in front of the impeller (that is just before they collide) a relationship between size and

velocity of impact was obtained. Assuming a particle velocity of  $1\text{ms}^{-1}$  at the inlet, figure 11 shows the particle velocities in front of the impeller, 1.51m downstream of the inlet of the domain. High-speed video observations of 50mm limestone particles indicated an average axial velocity component of  $10\text{m.s}^{-1}$  along the inlet duct; this limited information is in the same order as the predictions. The relationship of velocity with size is fitted with a Weibull function, with a correlation coefficient 0.997. It can be assumed that talc, with a Mohr's hardness index of 1, behaves in a similar way as limestone, for which Yashima et al (1987) provide plots of fracture energy versus particle size.

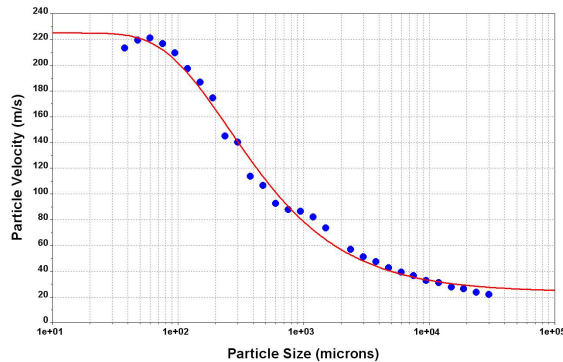


**Figure 11:** A Weibull function relates the particles velocity with their size at the impeller inlet.

Similarly, the specific and kinetic/fracture energy are shown in figure 12. To summarise, these are calculations be summing the kinetic energy change of all particles during their trajectories. They both show the steep increment of the energy requirement as the particle size descends.

The calculation of the number of impacts on all wall surfaces in the machine yielded the diagram in figure 13, which shows that the impeller is the area where most of the impacts happen. Therefore, one can say that the main breakage mechanism is impact, which is also suggested by observations of the rotor. However, validation of the numerical modelling and a better stochastic model is needed.

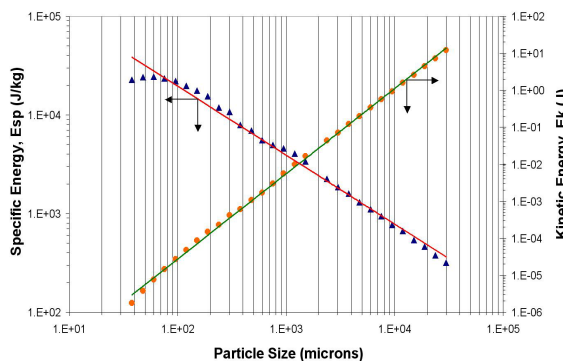


**Figure 12:** Specific and kinetic energy of talc particles at the inlet of the impeller zone.

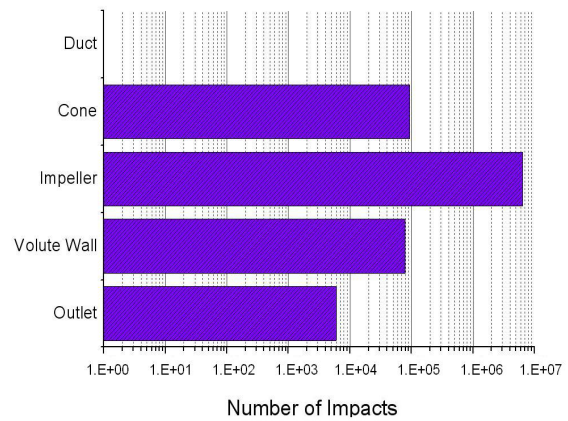


**Figure 13:** The particle-wall collisions in each zone of the domain indicate that the main breakage mechanism is impact.

Another mechanism is attrition, which is likely to occur at high throughput rates, and at the downstream of the device duct towards the cyclone.

From figure 4 the  $d_{80}$  values are  $10\ 000\mu\text{m}$  and  $80\mu\text{m}$  for the feed and the product, respectively. Figure 13, derives the specific energy for both size, which are 0.78 and 22.87kJ/kg, respectively. Subtracting the second from the first values, yielding the required specific energy in Bond law, which is 22.09 kJ/kg. Therefore, the Bond law, (McCabe et. al., 2001), is written in the form:

$$E_{sp} = 0.3162 W_i ((d_p/80)^{-0.5} - (d_F/80)^{-0.5}) \quad (34)$$

where feed and product sizes are in millimetres.

Thus, having a solid mass flow rate of  $1.0\text{kgs}^{-1}$ , one derives a Bond work index,  $W_i = 6.03\ \text{kWh}^{-1}$ . Because the grinding is assumed to be dry a correction factor of 4/3 (McCabe et al, 2001) applies to  $W_i$  to get the final value for Talc of the current case, which is  $W_i = 8.04\ \text{kWh}^{-1}$ .

This is a calculated characteristic value for the current material used, based on predicted values of numerical modelling. Further comparison with energy measurements of the apparatus might be difficult to taken due to the complex geometry.

As a first approach to the breakage mechanism the results are in agreement with physical observations, and justify the assumptions made as far as the numerical modelling is concerned. The modelling of irregular shape particles and the inter-particle collisions are important parameters for considerations for a complete breakage model. Moreover, a large number of trajectories will produce better visualisation of the physical phenomenon. An extra parameter to the modelling will be the diameter distributions derived from the Drop Weight Test.

## CONCLUSIONS

A new method of comminution was presented. Preliminary work has shown size reductions of up to 300:1 in fractions of a second, in a single pass. The identification of the flow structure and an understanding of the breakage mechanism are presented in the current paper using the CFD code FLUENT. A modified two-

equation  $k$ - $\epsilon$  turbulence model, RKE, used for the flow field solution, and results showed pleasing agreement with experimental measurements. However, owing to the anisotropy and inhomogeneity of the flow, the Reynolds Stress Model could be applied to improve the predicting. For two-phase flow using Talc, the Eulerian-Lagrangian stochastic model was used to predict the particle-wall impacts. The main assumptions in the model were that the particle diameter does not change and the particles shape is spherical. A proposed particle break model simulated a total number of 360 particles streams, at steady state, with modified profiles of restitution coefficients. Particle streams captured at the impeller inlet face and the kinetic energy were assumed to be equal to the required fracture energy. The energy input for each particle size was obtained and it will be the input parameter for using the Drop Weight Test method. From this method breakage distributions will be derived and further use of them will predict the actual breakage mechanism. The results proved that the main mechanism of breakage is impact and it occurs mostly in the impeller zone. Further impacts at the casing and outlet walls agree with experimental observations of the first author on the bended walls. Future work will include experimental profiles with more measured points at the boundary conditions, use of RSM model, tracking more particles streams, and the use of irregular shaped particles.

#### ACKNOWLEDGEMENTS

The primary author would like to acknowledge the financial support from Rio-Tinto and the European Commission framework 4 R&D Programme with acronym 'REFILL'. The presented material provided from Rio-Tinto Technology, UK and experimental work was carried out at Casella CRE Energy, Cheltenham. The work presented herein is part of the proposed thesis of the first author, and part of it has been presented in two European projects (ECSC 7220-PR083, and RC131). The authors acknowledge the collaboration and useful discussions with the inventors.

#### REFERENCES

- CHEN, X.-C., (2000), "Heavy particle dispersion in inhomogeneous, anisotropic, turbulent flows", *Int. J. Multiphase Flow*, 26, 635-661.
- CHEN, X.-Q., and Pereira, C.F., (1997), "Computational modelling of dilute gas-particle flows in an ultrasonic gas flowmeter", *J. Flow Measurements and Instrumentation*, 8, 167-182.
- CLIFT, R., GRACE, J.R., and Weber. M.E, (1978), "Bubbles, Drops, and Particles", Academic Press, Inc (London) Ltd, UK.
- COTTON, M.A., CRAFT, T.J., GUVY, A.W., and LAUNDER, B.E., (2001). "On modelling periodic motion with turbulence closure", *J. Flow Turbulence and Combustion*, 67, 143-158.
- FLUENT, MANUAL, 6.0 January 2002.
- MCCABE, L.W., SMITH, J.C., and HARRIOTT, P., (2001), "Unit operations of chemical engineering", 6<sup>th</sup> edition, McGraw-Hill, New York.
- PATENT GB 2354232 A, M.W. Youds et al, 21 March 2001.
- PATENT GB 2357499 A, M.W. Youds et al, 27 June 2001.

- PATENT GB 2358629 A, M.W. Youds, 01 August 2001.
- PATENT US 3,255,793 F. H. Clute, 14 June 1966.
- PATENT WO 9835756 A1, Next Century Technologies et al, 12 August 1998.
- PRASHER, C.L., (1987), "Crushing and grinding process handbook", John Wiley & Sons Ltd, UK.
- SCHLICHTING, H., (1979), "Boundary-Layer Theory", McGraw-Hill, New York.
- SHIH, T.-H., LIOU, W.W., SHABBIR, A., YANG, Z., and ZHU, J., (1995), "A New  $k$ - $\epsilon$  Eddy-Viscosity Model for High Reynolds Number Turbulent Flows - Model Development and Validation", *Computers Fluids*, 24, 3, 227-238.
- SOMMERFELD, M., and HO, C.A., (2003). "Numerical calculation of particle transport in turbulent wall bounded walls", *J. Powder Technology*, 131, 1-6.
- TABAKOFF, W., MALAK, M.F., and HAMED, A., (1987), "Laser measurements of solid-particles rebound parameters impacting on 2024 aluminium and 6A1-4V titanium alloys", *J. AIAA*, 25, 5, 721-726.
- TECHNICAL REPORT, (2002), ECSC 7220-PR083, "Optimised grinding of Coal".
- TECHNICAL REPORT, (2002), RC131, "Development of Novel Processing for the Production of Low-Cost By-Product Filters as a Replacement for High-Cost Primary Fillers – REFILL", MIRO UK, [www.miro.co.uk](http://www.miro.co.uk).
- WALLIN, S., and JOHANSSON, A.V., (2000), "An explicit algebraic Reynolds stress model for incompressible and compressible turbulent flows", *J. Fluid Mech.*, 403, 89-132.
- YASHIMA, S., KANDA, Y., and SANO, S., (1987), "Relationships between particle size and fracture energy or impact velocity required to fracture as estimated from single particle crushing", *J. Powder Technology*, 51, 277-282.